BOLETIN DE LA SOCIEDAD ESPAÑOLA DE
Cerámica y Vidrio
www.elsevier.es/bsecv

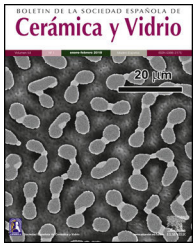

Study of the structural, ferroelectric and dielectric properties of $BaTiO_3$ co-doped with Sn^{4+} and Cr^{3+}

Fernando Daniel Cortés-Vega, Carlos Montero-Tavera, Jose Martin Yañez-Limón *

Center for Research and Advanced Studies of the National Polytechnic Institute, Querétaro Unit, Libramiento Norponiente No. 2000 Fracc. Real de Juriquilla, Querétaro, Qro., 76230 Querétaro, Mexico

ARTICLE INFO

Article history:
Received 11 November 2021
Accepted 23 March 2022
Available online 5 May 2022

Keywords:
Co-doping
Ferroelectric properties
Dielectric properties
Structural properties

ABSTRACT

In the present work, we studied the effect of Sn^{4+} and Cr^{3+} doping on the structural, ferroelectric, and dielectric properties of $BaSn_xCr_yTi_{1-(x+y)}O_3$. The materials were prepared by a combination of high-energy mechanical milling and solid-state reactions. The X-Ray Diffraction (XRD) analysis and Rietveld refinements confirmed the presence of a single tetragonal phase for the pure and doped samples. The SEM study revealed that the microstructure is highly susceptible to the addition of both dopants, causing an evident grain refinement. On the other hand, the addition of Sn^{4+} and Cr^{3+} had a strong influence on ferroelectric properties, as observed by the pinching of the ferroelectric hysteresis loops. The addition of Sn^{4+} increases the remnant and maximum polarization, as the Cr^{3+} doping promoted the contrary effect. Co-doping with Sn^{4+} and Cr^{3+} resulted in a maximum energy storage value of 0.2574 J/cm^3 with a efficiency of up to 65%, overcoming the values of pure BT. The relative permittivity of all doped samples remained in values of ~1000, just a little below the permittivity of pure BT.

Estudio de las propiedades estructurales, ferroeléctricas y dieléctricas de $BaTiO_3$ co-dopado conSn^{4+} y Cr^{3+}

Palabras clave:
Co-dopaje
Propiedades ferroeléctricas
Propiedades dieléctricas
Propiedades estructurales

RESUMEN

En el presente trabajo se estudiaron los efectos del co-dopaje con Sn^{4+} y Cr^{3+} en las propiedades estructurales, ferroeléctricas y dieléctricas de $BaSn_xCr_yTi_{1-(x+y)}O_3$. Los materiales se prepararon mediante una combinación de molienda mecánica de alta energía y reacciones en estado sólido. Los análisis de difracción de rayos X (DRX) y los refinamientos Rietveld confirmaron la presencia de únicamente la fase tetragonal tanto en la muestra de BT puro como en las dopadas. Los estudios realizados por microscopia electrónica de barrido revelaron que la microestructura de los materiales fabricados es altamente susceptible

* *Corresponding author.*
E-mail address: jmyanez@cinvestav.mx (J.M. Yañez-Limón).
https://doi.org/10.1016/j.bsecv.2022.03.002

a la adición de ambos dopantes, provocando un refinamiento considerable de tamaño de grano. Por otro lado, el dopaje con los iones Sn^{4+} y Cr^{+3} demostró tener una fuerte influencia en las propiedades ferroeléctricas, como se observó mediante la contracción de los ciclos de histéresis ferroeléctrica. La adición de Sn^{4+} incrementó los valores de polarización remanente y máxima, mientras que el dopaje con Cr^{3+} promovió el efecto contrario. El co-dopaje con Sn^{4+} y Cr^{3+} dio como resultado un valor máximo de almacenamiento de energía de 0,2574 J/cm^3 con una eficiencia de 65%, superando los valores de BT puro. La permitividad relativa de las muestras dopadas se mantuvo en valores de ∼1000, mostrando un decremento mínimo en comparación a la permitividad del BT puro.

Introduction

Nowadays, the use of ferroelectric ceramic materials to develop new technologies is an area of deep interest in the scientific and industrial sectors. The use of this class of materials is very wide, ranging from sensors and actuators to energy conversion and catalysis [1–3]. Furthermore, the use of lead-free ferroelectrics has attracted attention in the field of energy storage and more specifically, in advanced pulsed power capacitors due to their ability to release a high power density in a fast charge–discharge [4,5].

$BaTiO_3$ is one of the most important lead-free ferroelectric materials, and therefore, it has been the subject of several studies. Searching for the enhancement of the properties of $BaTiO_3$, it has been doped with multiple elements such as Bi, Fe, Li, Y, Nb, and Cr, as well as different rare-earth ions [6–12]. Particularly, Cr doped $BaTiO_3$ has been studied in regards to its catalytics properties. Chilukoti Srilakshmi et al. [13] synthesized $BaTiO_3$ doped with chromium by conventional oxalate and microwave assisted hydrothermal synthesis, achieving an improved performance in the conversion of nitrobenzene. Similar studies were carried out by I. C. Amaechi et al. [14] that reported on the synthesis of $BaTiO_3$ doped with Cr^{3+} in a range of 2–8 mol% by microwave-assisted method. Here was demonstrated the improvement in the photocatalytic performance of doped $BaTiO_3$ by photodegradation assessment of methyl orange, being ∼2.7 times higher than for the undoped material. Relevant results reported in the literature show that the incorporation of Cr in the BT allows maintaining the tetragonal structure up to concentrations in an atomic fraction of 0.03, and from 0.04 a pseudocubic phase can appear. On the other hand, the multivalent nature of Cr has also been detected when doping BT, found in Cr^{3+} and Cr^{5+} oxidation states [15].

The synthesis method is very important in the final crystalline structure of BT nanoparticles doped with Cr. C. Srilakshmi et al. [13] found that it is possible to obtain doped BT nanoparticles with Cr up to a concentration of 0.05 with a tetragonal or cubic structure, depending on whether a conventional oxalate hydrothermal method or a microwave-assisted method is used. The XPS results of the same authors show that oxidation states of Cr in BT matrix can occur in Cr^{3+} and Cr^{6+}. Additionally, studies of first principles by DFT [16] predict that Cr doping of the BT in its cubic phase should lead to an increase in the volume of the unit cell, in the brittleness of the ceramic, and a decreasing trend in the band-gap of the BT.

On the other hand, Tao Shi et al. [17] analyzed the influence of Sn^{4+} doping in $BaTiO_3$ by means of high resolution scanning transmission electron microscopy and first principles calculations. They determined that the presence of Sn^{4+} is responsible for the strong enhancement of dielectric permittivity and the presence of a diffuse phase transition in the doped material. Other researchers have also reported large enhancements of the piezoelectric and dielectric performance obtained by doping with Sn^{4+} [18,19].

W. Liu et al. [16] emphasize the general characteristics of the phase diagram of Sn-$BaTiO_3$. Among the effects of the doped BT with Sn are the decrease in T_C and the increase in the transition temperatures R–O and O–T. In such a way that for a concentration close to 11% of Sn, the 4 crystalline phases of BT coexist, R, O, T, and C, called quadruple point.

N. Horchidan et al. [20] studied the effects of BT doped with Sn, using several characterization techniques, finding that for concentrations less than 0.15 the tetragonal phase is obtained, and for concentrations greater than or equal to 0.20 the cubic phase is obtained. Additionally, the dielectric and Raman spectroscopy results indicate that at concentrations of 0.05 there is a coexistence of phases O and T, and at 0.15 there is a coexistence of T and C phases. Also, the introduction of Sn induces the appearance of polar nano-regions related to the relaxor behavior of the BST system. Li et al. [21] reported the synthesis of BT doped with Sn under an H_2–N_2 mixture atmosphere, obtaining a very large dielectric constant at room temperature (1.2×10^4 at 1 kHz), as well as dielectric losses close to 1% and resistivities of the order of tens of MΩ cm.

However, to the best of our knowledge the combination of these dopants has not been reported previously, and therefore, there is no information about the behavior and properties of this co-doped system.

In this work, we present the study of ferroelectric, dielectric and structural properties of $BaTiO_3$ (BT) co-doped with Sn^{4+} and Cr^{3+}, as well as the analysis of the evolution of the ferroelectric–paraelectric transition from a typical Curie-Weiss behavior to partial diffuse transition. The obtained results represent novel and useful information for the development and better understanding of new ferroelectric systems.

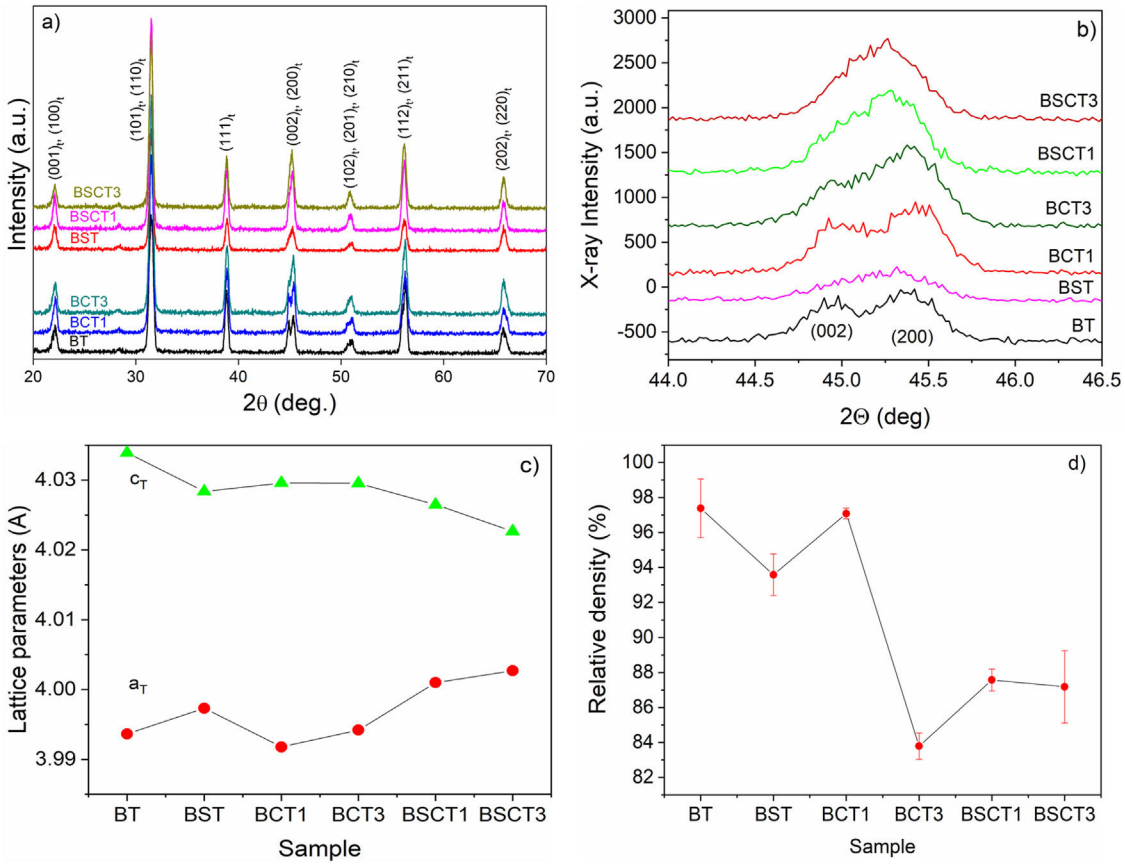

Fig. 1 – (a) XRD patterns in the 2θ range of 20–70°, (b) amplification of XRD patterns in the range of 44–46°, (c) lattice parameters estimated by Rietveld refinement and (d) relative density measurements.

Experimental procedure

Materials

Barium carbonate ($BaCO_3$; ≥99% purity), titanium dioxide (TiO_2; 99.5% purity), tin oxide (SnO_2; 99.9% purity) and chromium oxide (Cr_2O_3; ≥98%) were purchased from Sigma–Aldrich.

Processing and synthesis

The starting powders were mixed using a high-energy mill SPEX 8000 according to the following compositions: $BaTiO_3$ (BT), $BaCr_{0.01}Ti_{1-(0.01)}O_3$ (BCT1), $BaCr_{0.03}Ti_{1-(0.03)}O_3$ (BCT3), $BaSn_{0.02}Cr_{0.01}Ti_{1-(0.03)}O_3$ (BSCT1), $BaSn_{0.02}Cr_{0.03}Ti_{1-(0.05)}O_3$ (BSCT3) and $BaSn_{0.02}Cr_{0.00}Ti_{1-(0.02)}O_3$ (BST). The milling time for each composition was 2 h, using zirconia balls with different diameters. The ratio of zirconia balls was 2:10 with diameters of 10 and 6 mm, respectively. The mixtures of powders resulting from the milling stages were calcined at 1100 °C for 2 h, and then, grinded in a mortar and compacted in cylindrical pellets of 10 mm of diameter at a pressure of 193.11 MPa. The cylindrical pellets were densified at 1300 °C for 2 h in air atmosphere. After sintering, the density of all samples was estimated by Archimedes principle.

Characterization

The crystalline structure of the prepared materials was analyzed using a Rigaku D_{max}-2100 diffractometer with a Bragg–Brentano geometry and Cu-Kα radiation (λ = 1.5418 Å) at step size = 0.02, t = 0.3 s, and 20°–70° in 2θ range. The study of the surface microstructure was carried out with a field emission Philips XL30 ESEM microscope working at 15 kV and with secondary electrons detector. All the samples were previously polished and coated with a thin layer of gold, using a coater machine Denton Vacuum desk V.

The grain size was calculated by measuring the diameter of 100 single grains for each sample using the free software ImageJ. Ferroelectric characterization was performed using an equipment from Radiant Technologies Inc. with a coupled external high-voltage amplifier (4000 V) TREK model 609-6 at 200 Hz (5 ms) and using a triangle waveform. The dielectric properties were measured with a KEYSIGHT E499A impedance analyzer operating at a frequency range of 20 Hz to 10 MHz. The impedance analyzer is coupled to a homemade oven that allows temperature measurements in a range of 25–300 °C.

Results and discussion

Fig. 1a–d shows the XRD patterns, lattice parameters and relative density of the investigated samples. The XRD patterns for

Table 1 – Parameters obtained by Rietveld refinement.

BT	BST	BCT1
sigma = 2.458	sigma = 2.251	sigma = 2.293
R_{wp} (%) = 21.37	R_{wp} (%) = 24.35	R_{wp} (%) = 19.32
R_b (%) = 17.355	R_b (%) = 18.25	R_b (%) = 14.87
R_{exp} (%) = 8.69	R_{exp} (%) = 10.82	R_{exp} (%) = 8.43
$a = 3.9936 \pm 6.3E{-}4$	$a = 3.9973 \pm 7.9E{-}4$	$a = 3.9918 \pm 4.6E{-}4$
$c = 4.0339 \pm 7.4E{-}4$	$c = 4.0283 \pm 9.7E{-}4$	$c = 4.0296 \pm 5.8E{-}4$
BCT3	**BSCT1**	**BSCT3**
sigma = 2.231	sigma = 2.189	sigma = 2.2814
R_{wp} (%) = 17.35	R_{wp} (%) = 18.73	R_{wp} (%) = 20.44
R_b (%) = 13.25	R_b (%) = 14.33	R_b (%) = 15.82
R_{exp} (%) = 7.77	R_{exp} (%) = 8.55	R_{exp} (%) = 8.96
$a = 3.9942 \pm 5.1E{-}4$	$a = 4.0009 \pm 4.9E{-}4$	$a = 4.0026 \pm 5.7E{-}4$
$c = 4.0295 \pm 6.2E{-}4$	$c = 4.0264 \pm 6.6E{-}4$	$c = 4.0226 \pm 9.1E{-}4$

all the investigated samples are shown in Fig. 1a. The Rietveld refinement made using the software MAUD [22] confirmed the presence of a single tetragonal phase for all sample compositions, the R_{wp} values obtained in the fitting to XRD patterns of our set of samples are in a range between 17 and 24%, and sigma values are between 2.18 and 2.45. In Table 1 are listed the resulting parameters of the Rietveld refinement for all the studied samples. In addition, the good fitting achieved from the Rietveld Refinement for the sample BT can be found in the supplementary material (see Fig. S1). Further evidence of the presence of a tetragonal phase may be observed in Fig. 1a. Here, we can see the presence of the characteristic tetragonal planes (002) and (200) for all the processed samples [23] PDF#05-0626. The evolution of the lattice parameters with doping is observed in Fig. 1c. On the one hand, the parameter c_T tends to slightly decrease with doping when compared with pure BT. In contrast, the parameter a_T increases with doping, and therefore, decreases the tetragonality degree. The relative density for each sample is observed in Fig. 1d. The obtained values suggest that the addition of doping atoms hinders the densification process to a certain degree as we observe a decrease in the relative density in all cases, except by the sample BCT1. The highest relative density was observed for pure BT (97.3%), whereas the lowest density values were found for the sample BCT3 (83.8%).

In Fig. 2 the SEM images of pure and doped materials are displayed, which correspond to the surface of the as densified samples. Comparatively, all doped samples exhibit a significant grain refinement to a different extent, according to the amount and type of dopant added. The grain size measurements were carried out by measuring the diameter of the grains. Likewise, the average values are plotted in Fig. 3. The sample with the largest grain size was BT with an average diameter of $98.8 \pm 15\,\mu m$, whereas the samples that showed the lowest diameter values were BCT3 and BSCT3, with diameter of 4.6 ± 1.5 and $2.6 \pm 0.5\,\mu m$.

The relative permittivity of samples is plotted in Fig. 4 in a temperature range of 25–300 °C. The maximum relative permittivity point that belongs to the ferroelectric–paraelectric (F–P) transition shows slight shifts to a lower temperature with the addition of dopants. These shifts exhibit a maximum value for the samples BSCT1 and BSCT3, being 113.17 and 113.34 °C, respectively. However, the most prominent effect of temperature reduction on the F–P transition is attributed

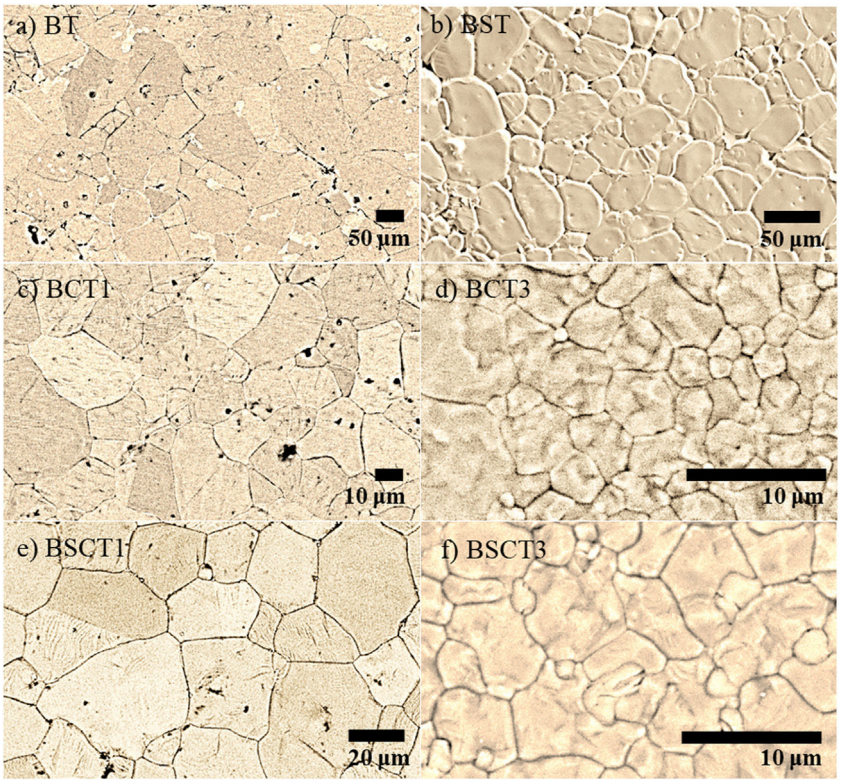

Fig. 2 – SEM images of surface microstructure for pure and doped samples. (a) BT, (b) BST, (c) BCT1, (d) BCT3, (e) BSCT1, and (f) BSCT3.

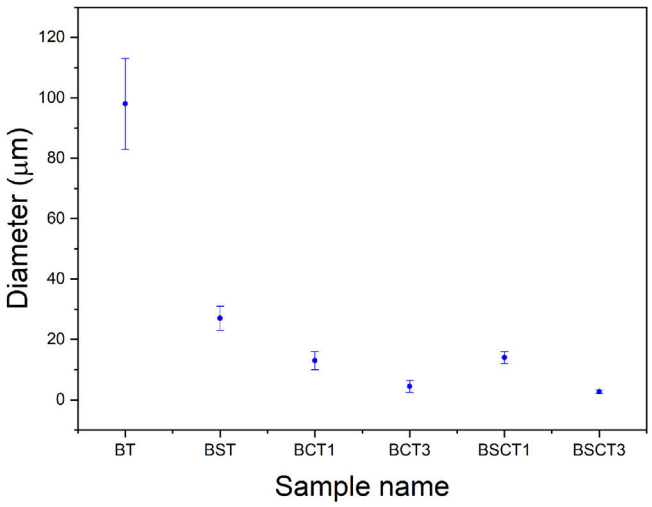

Fig. 3 – Grain size measurements.

to the single addition of Sn^{4+} in the BST sample, whereas the influence of Cr^{3+} is minimal. In good agreement with our results, we observed that the addition of Sn decreases the temperature of the F–P transition. Md. Jawed and Shail Upadhyay [24], studied the effect of 0.05 and 0.15 additions of Sn into the $BaTiO_3$ structure. They reported significant reductions of the F–P temperature going from 123 °C for pure $BaTiO_3$ and up to 10 °C for the sample with higher amount of Sn. Similar trends were observed by C. Kajtoch in his study of the dielectric properties of $BaTiSnO_3$ ceramics. Here, it was observed that the increase of Sn concentration in the range of 0.05–0.20 (molar fraction) strongly lowers the F–P transition [25]. Remarkably, the relative permittivity before the temperature transition remains very similar among pure and doped samples, without showing a significant reduction. Here, we can see that pure BT has a relative permittivity around 1200 before the F–P transition, whilst the BST, BCT3, and BSCT3 samples exhibit similar values above 1000. The samples with the lowest concentrations of dopants (BCT1 and BSCT1) show a slight decrease in the relative permittivity values. The dispersion of relative permittivity as a function of frequency may be explained in terms of interfacial polarization. Here, we consider that the volume of the grains is a conductive zone that allows the free flow of charges under the influence of an external electrical field, whereas the grain boundaries may be seen as poor or null conductive zones [26–28]. Therefore, free charges move readily in the inner of the grains and accumulate on the grain boundaries, generating an interfacial polarization. Thus, when the applied field is of low frequency, the movement of charges takes place readily, whereas, with the increase of frequency, the free charges are not able to follow the applied electric field.

In the supplementary material, the behavior analysis of the dielectric function with temperature is presented in terms of

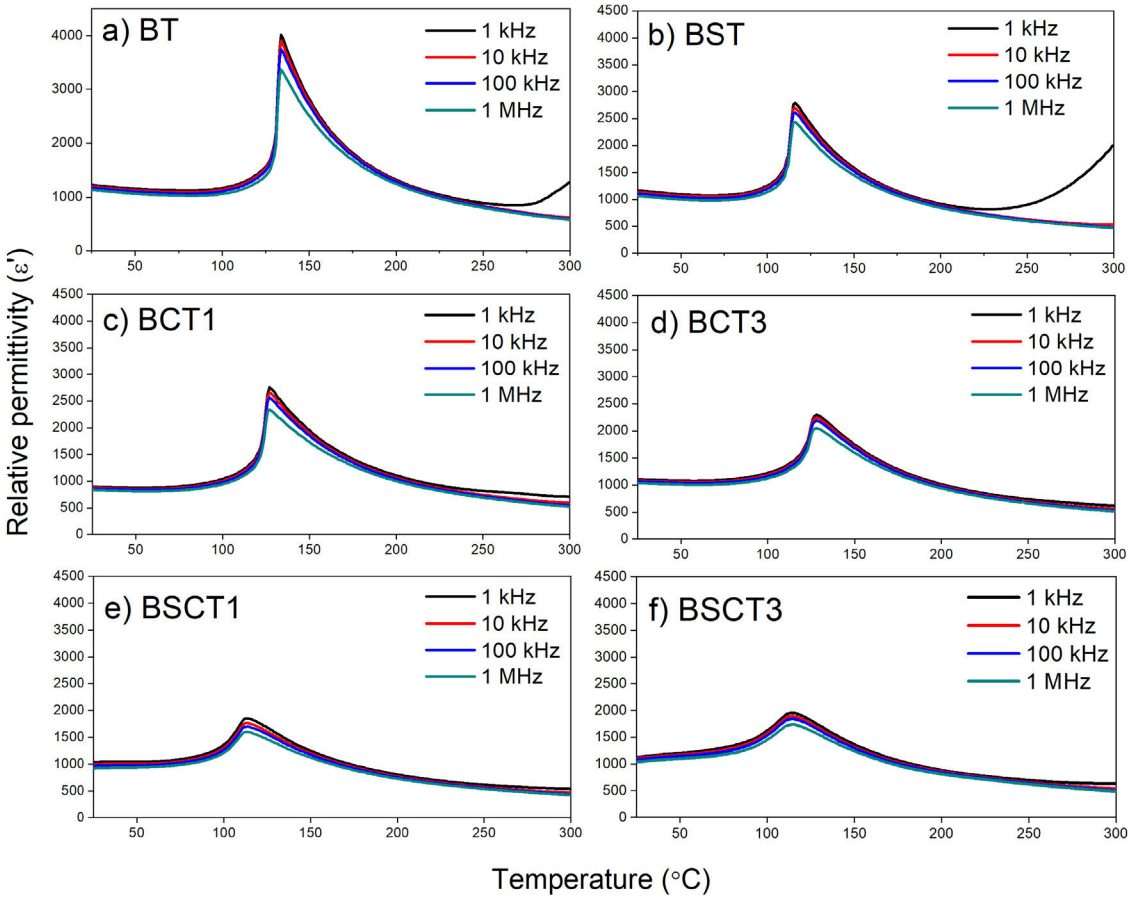

Fig. 4 – Relative permittivity (ε′) measurements of processed samples at different frequencies. (a) BT, (b) BST, (c) BCT1, (d) BCT3, (e) BSCT1 and (f) BSCT3.

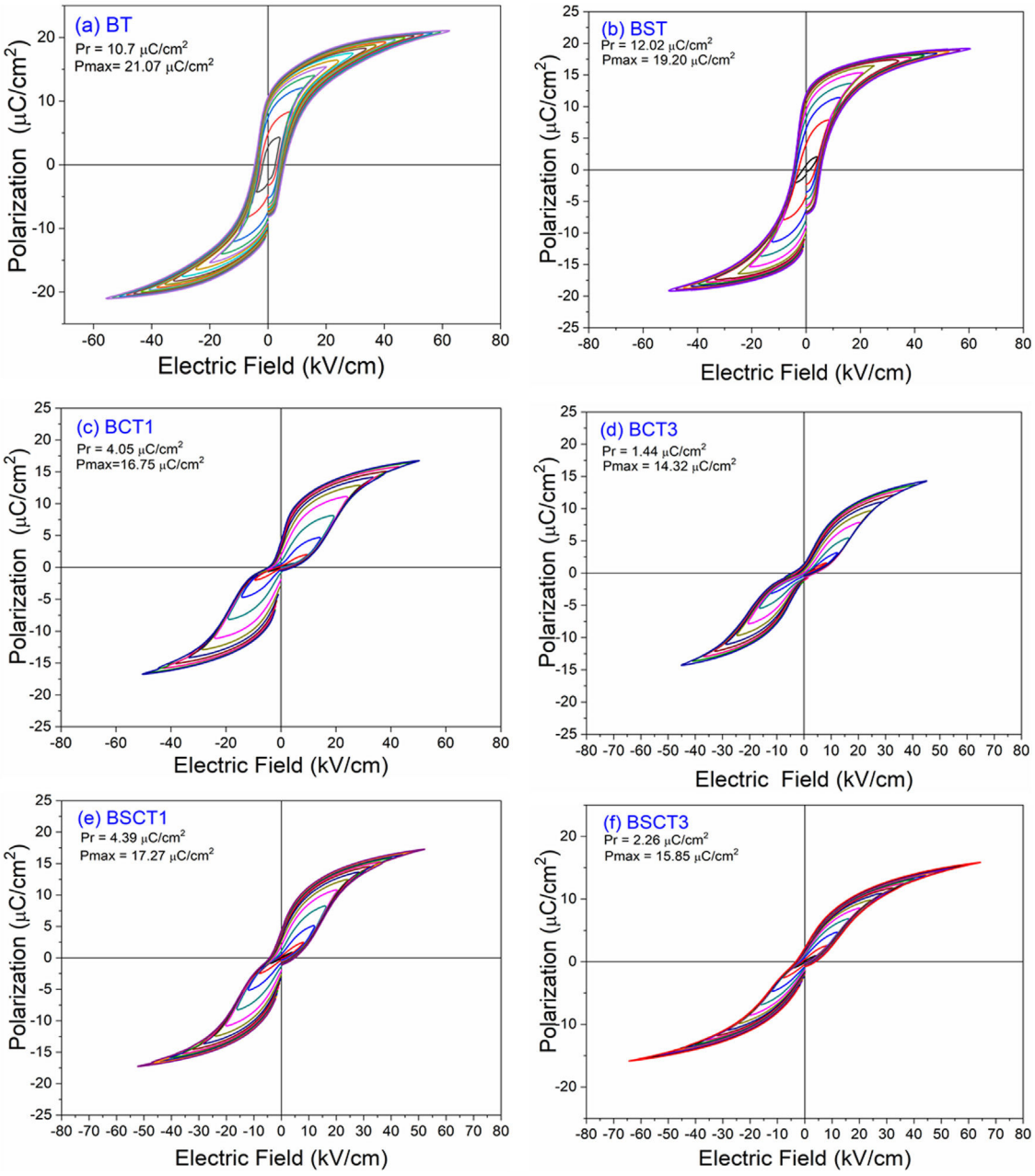

Fig. 5 – Ferroelectric hysteresis loops for pure BT and doped samples measured at a frequency of 200 Hz.

the Curie Weiss and Uchino-Nomura models. Through the latter, it is possible to determine the degree of diffuseness of the F–P transition, Figs. S1, and S2. The parameters obtained are presented in table S1. The results show that the highest values of diffuseness coefficient (γ) were obtained for the samples BSCT1 and BSCT3, being 1.4458 ± 0.0115 and 1.6143 ± 0.0143, respectively. The high values of γ for the samples BSCT1 and BSCT3 are attributed to the type and concentration of added dopants that generates fluctuations in the chemical composition, formation of crystal defects, and therefore, an increase of the structural disorder that leads to the formation of a broad or diffuse phase transition [20].

The results of dielectric losses are shown in the supplementary material Fig. S3. It can be seen that the dielectric losses are less than 0.5 in all the samples up to 200 °C. At higher temperatures an increase in dielectric losses is observed, reaching values close to 1.5 for the BT and BST samples, the samples with Cr do not exceed 0.3 at 300 °C. This increase in dielectric losses can be associated with the thermal activation of the different types of defects present in the samples, such as oxygen vacancies and charge imbalance sites due to the presence of Cr^{3+} and possibly Cr^{6+}. However, the fact that they are lower in samples with Cr is also an indication that in this range of low dopant concentrations, the action of the dopant is to compensate for the native vacancies of oxygen present in BT and BST.

The behavior of the ferroelectric hysteresis loops for all the samples is presented in Fig. 5. Here, we can appreciate the

Table 2 – Values of remnant and maximum polarization for processed samples.

Sample	P_r	P_{max}	Sample	P_r	P_{max}
BT	10.7	21.07	BST	12.02	19.2
BCT1	4.05	16.75	BSCT1	4.39	17.27
BCT3	1.44	14.32	BSCT3	2.26	15.85

Table 3 – Energy storage density.

Sample	Energy storage density (J/cm^3)	Efficiency (%)
BT	0.1609	35
BST	0.1130	31
BSCT1	0.1814	49
BSCT3	0.2574	65
BCT1	0.1565	40
BCT3	0.1724	56

strong influence of Sn^{4+} and Cr^{3+} co-doping on the ferroelectric properties. Initially, the pure BT observed in Fig. 4a shows a typical ferroelectric hysteresis loop with values of 10.7 μC/cm^2 and 21.07 μC/cm^2 for the remnant (P_r) and maximum (P_{max}) polarization, respectively. Comparatively, the addition of Sn^{4+} in the sample BST0 boosted the value of P_r up to 12.02 μC/cm^2 but slightly deteriorated the P_{max} (see Table 2). Similar results have been found in previous reports, showing increments of P_r with the addition of Sn^{4+}, maintaining a typical ferroelectric hysteresis loop [18,29]. Except for sample BST, all other compositions show a strong reduction of remnant polarization (see Table 2). The addition of Cr^{3+} promoted the appearance of double hysteresis loops as observed in Fig. 5b and c for samples BCT1 and BCT3, respectively. With the increase of the Cr^{3+} concentration from BCT1 to BCT3, there is a constriction of the hysteresis loops, as well as a considerable reduction in P_r and P_{max}. We consider that the pinched form of the hysteresis loops observed in samples doped with Cr is very likely to be related to local charged defects induced by Cr^{3+} that replaces Ti and causes imbalances of charge in the oxygen octahedron. Additionally, it has also been reported that Cr may be also present as Cr^{5+} and Cr^{6+} oxidation states [13,15], which would induce larger amount of defects. The presence of Cr^{3+} and Cr^{6+} together have a similar effect to that observed for Pb–O in PZT, which act as pinning centers of the domain walls and give rise to the pinched shape of the hysteresis loops. We rule out a dominant contribution of Sn-induced polar nano regions, since a low concentration of Sn, 0.02 in atomic fraction, is used in all samples, and in this concentration range the relaxor effects associated with Sn are not expected.

In general, it is observed that the addition of only Sn^{4+} enhances the value of P_{max} as the addition of Cr^{3+} decreases the P_r, promoting the formation of slim loops. Given the characteristic of presenting low values of P_r, it is interesting to estimate the recoverable energy storage capacity and storage efficiency [30] for all materials as displayed in Table 3.

The highest values of recoverable energy storage and efficiency were found for BSCT3 sample, being 0.2574 J/cm^3 and 65%, respectively. These values represent a significant improvement in comparison to those observed for pure BT (Energy storage density = 0.1609 J/cm^3 and Storage efficiency = 35%). However, the energy storage capacities calculated in this work are lower than others observed for systems as $Bi_{0.5}Na_{0.5}TiO_3$–$BaTiO_3$–$SrTi_{0.875}Nb_{0.1}O_3$, $Pb(Zr_{0.95}Ti_{0.05})_{0.98}Nb_{0.02}O_3$ and $0.9Pb(Mg_{1/3}Nb_{2/3})O_3$–$0.1PbTiO_3$ that have reported values of 1.17 [31], 3.0 [32] and 9.8 J/cm^3 [33], respectively.

Conclusions

In this study, the results of the ferroelectric, dielectric, and structural characterization of the lead-free ferroelectric $BaTiO_3$ co-doped with Sn^{4+} and Cr^{3+} have been reported. The addition of both dopants demonstrated to have a strong influence on the physical properties of the host structure. It was observed that the microstructure of doped samples suffered a notable grain refinement and, at the same time, the XRD analysis revealed the presence of a single tetragonal phase for all compositions. The pinching effect of the ferroelectric hysteresis loops might be associated to local charged defects induced by the addition of Cr that is likely to be present in different valence states. The energy storage density and efficiency of the samples increased in all cases except for the sample BST, achieving the best performance for the sample BSCT3.

Acknowledgements

This work was financially supported by the Projects CB 240460, LIDTRA LN2015-254119, and LN2021-315906 of CONACYT. The authors thank the National Laboratory, LIDTRA, for the infrastructure facilities provided for the realization of this work. F.D. Cortes Vega and C. Montero-Tavera are grateful to CONACYT for the scholarships granted for postdoctoral stays and doctoral studies, respectively. Also, the authors want to thank the support provided by the laboratory technicians, Adair Jimenez Nieto, Rivelino Flores Farias, Martín Adelaido Hernández Landaverde, and Agustín Galindo Sifuentes.

Appendix A. Supplementary data

Supplementary data associated with this article can be found, in the online version, at doi:10.1016/j.bsecv.2022.03.002.

REFERENCES

[1] A.K. Bain, P. Chand, Ferroelectric ceramics: devices and applications, Ferroelectrics (2017) 195–306, http://dx.doi.org/10.1002/9783527805310.ch5.
[2] I. Chilibon, J.N. Marat-Mendes, Ferroelectric ceramics by sol–gel methods and applications: a review, J. Sol-Gel Sci. Technol. 64 (2012) 571–611, http://dx.doi.org/10.1007/s10971-012-2891-7.
[3] R. Whatmore, Ferroelectric materials, in: S. Kasap, P. Capper (Eds.), Springer Handbook of Electronic and Photonic Materials, Springer International Publishing, Cham, 2017, p. 1, http://dx.doi.org/10.1007/978-3-319-48933-9_26.
[4] K. Han, N. Luo, S. Mao, F. Zhuo, L. Liu, B. Peng, X. Chen, C. Hu, H. Zhou, Y. Wei, Ultrahigh energy-storage density in A-/B-site co-doped $AgNbO_3$ lead-free antiferroelectric ceramics: insight into origin of antiferroelectricity, J. Mater. Chem. A 3 (2019) 1–9, http://dx.doi.org/10.1039/c9ta06457e.

[5] H. Pan, Y. Zeng, Y. Shen, Y.H. Lin, J. Ma, L. Li, C.W. Nan, $BiFeO_3$–$SrTiO_3$ thin film as a new lead-free relaxor-ferroelectric capacitor with ultrahigh energy storage performance, J. Mater. Chem. A 5 (2017) 5920–5926, http://dx.doi.org/10.1039/c7ta00665a.
[6] W.B. Li, D. Zhou, L.X. Pang, R. Xu, H.H. Guo, Novel barium titanate based capacitors with high energy density and fast discharge performance, J. Mater. Chem. A 5 (2017) 19607–19612, http://dx.doi.org/10.1039/c7ta05392d.
[7] Z. Shen, X. Wang, B. Luo, L. Li, $BaTiO_3$–$BiYbO_3$ perovskite materials for energy storage applications, J. Mater. Chem. A 3 (2015) 18146–18153, http://dx.doi.org/10.1039/c5ta03614c.
[8] M.J. Wang, H. Yang, Q.L. Zhang, Z.S. Lin, Z.S. Zhang, D. Yu, L. Hu, Microstructure and dielectric properties of $BaTiO_3$ ceramic doped with yttrium, magnesium, gallium and silicon for AC capacitor application, Mater. Res. Bull. 60 (2014) 485–491, http://dx.doi.org/10.1016/j.materresbull.2014.09.023.
[9] J. Huang, J. Zhang, H. Yu, M. Wei, H. Chen, C. Yang, Improvement of dielectric and energy storage properties in $BaTiO_3$ ceramics with $BiNbO_4$ modified, Ferroelectrics 510 (2017) 8–15, http://dx.doi.org/10.1080/00150193.2017.1325709.
[10] H.T. Langhammer, T. Müller, R. Böttcher, H.P. Abicht, Structural and optical properties of chromium-doped hexagonal barium titanate ceramics, J. Phys. Condens. Matter 20 (2008), http://dx.doi.org/10.1088/0953-8984/20/8/085206.
[11] S. Madolappa, R. Sagar, R.L. Raibagkar, Synthesis, structural and electrical investigations of Gd-and Cr-Doped $BaTiO_3$ nanoparticle ceramics, Ferroelectrics 413 (2011) 37–45, http://dx.doi.org/10.1080/00150193.2011.542699.
[12] J. Shah, R.K. Kotnala, Induced magnetism and magnetoelectric coupling in ferroelectric $BaTiO_3$ by Cr-doping synthesized by a facile chemical route, J. Mater. Chem. A 1 (2013) 8601–8608, http://dx.doi.org/10.1039/c3ta1 1845.
[13] C. Srilakshmi, R. Saraf, V. Prashanth, G.M. Rao, C. Shivakumara, Structure and catalytic activity of Cr-doped $BaTiO_3$ nanocatalysts synthesized by conventional oxalate and microwave assisted hydrothermal methods, Inorgan. Chem. 55 (2016) 4795–4805, http://dx.doi.org/10.1021/acs.inorgchem.6b00240.
[14] I.C. Amaechi, G. Kolhatkar, A.H. Youssef, D. Rawach, S. Sun, A. Ruediger, B-site modified photoferroic Cr^{3+}-doped barium titanate nanoparticles: microwave-assisted hydrothermal synthesis, photocatalytic and electrochemical properties, RSC Adv. 9 (2019) 20806–20817, http://dx.doi.org/10.1039/c9ra03439k.
[15] D.-Y. Lu, Y. Liang, Valence states and dielectric properties of fine-grained $BaTiO_3$ ceramics co-doped with double valence-variable europium and chromium, Ceram. Int. 44 (2018) 14717–14727, http://dx.doi.org/10.1016/j.ceramint.2018.05.100.
[16] K.M. Hossain, S. Ahmad, S.K. Mitro, Physical properties of chromium-doped barium titanate: effects of chromium incorporation, Phys. B: Condens. Matter 626 (2022) 413494, http://dx.doi.org/10.1016/j.physb.2021.413494.
[17] T. Shi, L. Xie, L. Gu, J. Zhu, Why Sn doping significantly enhances the dielectric properties of $Ba(Ti_{1-x}Sn_x)O_3$, Sci. Rep. 5 (2015) 8–11, http://dx.doi.org/10.1038/srep08606.
[18] W. Liu, J. Wang, X. Ke, S. Li, Large piezoelectric performance of Sn doped $BaTiO_3$ ceramics deviating from quadruple point, J. Alloys Compd. 712 (2017) 1–6, http://dx.doi.org/10.1016/j.jallcom.2017.04.013.
[19] S. Gattu, K.S. Dasari, V.R. Kocharlakota, Structural and dielectric properties of sn doped barium magnesuim zirconium titanate perovskite ceramics, World J. Condens. Matter Phys. 05 (2015) 346–352, http://dx.doi.org/10.4236/wjcmp.2015.54035.
[20] N. Horchidan, A.C. Ianculescu, C.A. Vasilescu, M. Deluca, V. Musteata, H. Ursic, R. Frunza, B. Malic, L. Mitoseriu, Multiscale study of ferroelectric–relaxor crossover in $BaSn_xTi_{1-x}O_3$ ceramics, J. Eur. Ceram. Soc. 34 (2014) 3661–3674, http://dx.doi.org/10.1016/j.jeurceramsoc.2014.06.005.
[21] L. Li, R. Wang, S. Yu, Z. Sun, H. Zheng, Novel tin-doped $BaTiO_3$ ceramics with non-reducibility and colossal dielectric constant, Mater. Lett. 220 (2018) 119–121, http://dx.doi.org/10.1016/j.matlet.2018.03.015.
[22] M. Ferrari, L. Lutterotti, Method for the simultaneous determination of anisotropic residual stresses and texture by X-ray diffraction, J. Appl. Phys. 76 (1995) 7246–7255, http://dx.doi.org/10.1063/1.358006.
[23] D.-H. Yoon, Tetragonality of barium titanate powder for a ceramic capacitor application, J. Ceram. Process. Res. 7 (2006) 343–354.
[24] M.J. Ansaree, S. Upadhyay, Study of phase evolution and dielectric properties of Sn-doped barium titanate, Emerg. Mater. Res. 6 (2017) 21–28, http://dx.doi.org/10.1680/jemmr.16.00013.
[25] C. Kajtoch, Dielectric properties of Ba $(Ti_{1-x}Sn_x)O_3$ ceramics in the paraelectric phase, Ceram. Int. 37 (2011) 387–391, http://dx.doi.org/10.1016/j.ceramint.2010.07.006.
[26] J. Sharma, J. Parashar, V.K. Saxena, D. Bhatnagar, K.B. Sharma, Study of dielectric properties of nanocrystalline cobalt ferrite upto microwave frequencies, Macromol. Symp. 357 (2015) 38–42, http://dx.doi.org/10.1002/masy.201400183.
[27] S.A. Mazen, N.I. Abu-elsaad, Structural, magnetic and electrical properties of the lithium ferrite obtained by ball milling and heat treatment, Appl. Neurosci. 3 (2015) 105–114, http://dx.doi.org/10.1007/s13204-014-0297-2.
[28] C. Rayssi, S. El Kossi, J. Dhahri, K. Khirouni, Frequency and temperature-dependence of dielectric permittivity and electric modulus studies of the solid solution $Ca_{0.85}Er_{0.1}Ti_{1-x}Co_{4x/3}O_3$ $(0 \leq x \leq 0.1)$, RSC Adv. 8 (2018) 17139–17150, http://dx.doi.org/10.1039/c8ra00794b.
[29] S.K. Upadhyay, P. Bag, Electro-caloric effect in lead-free Sn doped $BaTiO_3$ ceramics at room temperature and low applied fields Electro-caloric effect in lead-free Sn doped $BaTiO_3$ ceramics at room temperature and low applied fields Sanjay Kumar Upadhyay, V. Raghavendra Reddy (2014), http://dx.doi.org/10.1063/1.4896044.
[30] L. Zhao, Q. Liu, S. Zhang, J.F. Li, Lead-free $AgNbO_3$ anti-ferroelectric ceramics with an enhanced energy storage performance using MnO_2 modification, J. Mater. Chem. C 4 (2016) 8380–8384, http://dx.doi.org/10.1039/c6tc03289c.
[31] J. Shi, X. Liu, W. Tian, High energy-storage properties of $Bi_{0.5}Na_{0.5}TiO_3$–$BaTiO_3$–$SrTi_{0.875}Nb_{0.1}O_3$ lead-free relaxor ferroelectrics, J. Mater. Sci. Technol. 34 (2018) 2371–2374, http://dx.doi.org/10.1016/j.jmst.2018.06.008.
[32] S.I. Shkuratov, J. Baird, V.G. Antipov, S. Zhang, J.B. Chase, Multilayer PZT 95/5 antiferroelectric film energy storage devices with giant power density, Adv. Mater. 31 (2019) 1904819, http://dx.doi.org/10.1002/adma.201904819.
[33] M. Sadl, O. Condurache, A. Bencan, M. Dragomir, U. Prah, B. Malic, M. Deluca, U. Eckstein, D. Hausmann, N.H. Khansur, K.G. Webber, H. Ursic, Energy-storage-efficient $0.9Pb(Mg_{1/3}Nb_{2/3})O_3-0.1PbTiO_3$ thick films integrated directly onto stainless steel, Acta Mater. 221 (2021) 117403, http://dx.doi.org/10.1016/j.actamat.2021.117403.